



Cite this: *RSC Adv.*, 2025, 15, 16814

Preparation and synergistic effect of aluminum hydroxide nanoplates on the fire resistance and thermal stability of the intumescent flame retardant epoxy composite

Truong Cong Doanh,^a Nhung Hac Thi,^{bc} Hong Tham Nguyen,^b Ho Thi Oanh,^b Tien Dat Doan,^{bc} Nguyen Duc Tuyen,^b Minh-Tan Vu^a and Mai Ha Hoang ^{*bc}

Aluminum hydroxide nanoplates (nATH), with an average particle size of about 350–450 nm and a thickness of 30 nm, were successfully synthesized through a hydrothermal process using an $\text{Al}(\text{OH})_3$ gel precursor. The ATH nanoplates were then surface-treated with organic compounds and incorporated into an intumescent flame-retardant epoxy system containing polyethyleneimine-modified ammonium polyphosphate (APP@PEI). Among them, the combination of APP@PEI and PEI-treated nATH (nATH_{PEI}) exhibited the highest synergistic effect on the fire resistance and thermal stability of epoxy resin due to the superior dispersion of the nanoplates. Additionally, the optimal mass ratio of two flame retardant additives was examined. As a result, a nanocomposite containing 3 wt% nATH_{PEI} and 7 wt% APP@PEI exhibited the best flame resistance and thermal-oxidative stability. This nanocomposite reached a V-0 rating in the UL-94 vertical burning test with a high limiting oxygen index value of 31.1%, and a substantial char yield of 17.98% at 900 °C. Char residues of samples were analyzed by Fourier transform infrared spectroscopy, X-ray diffraction, and scanning electron microscopy coupled with energy dispersive X-ray analysis to investigate the reasonable flame retardant mechanism. The results demonstrated that the formation of highly thermally stable aluminum phosphates played an important role in the augmentation of the flame retardancy in the condensed phase. Furthermore, tension and Izod impact tests indicated that the presence of nATH_{PEI} notably increased the mechanical properties of composite loading APP@PEI. This combination provides a promising approach for intumescent flame retardant applications in epoxy resin.

Received 10th January 2025
Accepted 12th May 2025

DOI: 10.1039/d5ra00231a

rsc.li/rsc-advances

1 Introduction

Epoxy resin (EP), a type of thermosetting resin, has attracted conspicuous attention for the last decades because of its great solvent resistance, high mechanical strength, superior adhesion, excellent electrical insulation, low shrinkage, easy processing, and low cost. Hence, EP has been widely applied in several fields, including electronic and electrical materials, binders, coatings, and fiber-reinforced composite materials.^{1–3} However, its flammability remains a major disadvantage, severely restricting its potential for further application. Thus, it is essential to improve the flame retardancy of EP resin. In recent years, researchers have developed various solutions to address this issue. Among them, the introduction of flame

retardant additives is one of the most effective approaches to enhance the fire resistance of EP resin.^{4–8}

Intumescent flame retardants (IFRs), an important class of halogen-free flame retardant materials, offer several significant benefits, such as non-toxicity, low smoke emission, and resistance to dripping.⁹ Typically, IFRs include three main components: acid, carbon, and gas sources.¹⁰ IFRs form a voluminous intumescent char layer that insulates heat and oxygen, effectively protecting underlying polymer matrices from flames. Ammonium polyphosphate (APP), a crucial phosphorus-based flame retardant, serves as an acid source in IFR formulations. This flame retardant often has excellent char-forming effects when combined with other components.^{11–14} However, APP often has poor dispersibility and compatibility with polymer matrices, which can negatively impact mechanical properties of polymers, thereby hindering its performance in engineering applications. In recent years, many efforts have been focused on investigating APP-based IFR systems.^{8,15–18} Meanwhile, APP modified with hyperbranched polyethyleneimine (APP@PEI) which acts as a hardener for thermosets,^{19,20} is considered an effective IFR system for EP resins.

^aHanoi University of Industry, 298 Cau Dien, Bac Tu Liem, Hanoi, 12000, Vietnam

^bInstitute of Chemistry, Vietnam Academy of Science and Technology, 18 Hoang Quoc Viet, Cau Giay, Hanoi, 10072, Vietnam. E-mail: hoangmaiha@ich.vast.vn

^cGraduate University of Science and Technology, Vietnam Academy of Science and Technology, 18 Hoang Quoc Viet, Cau Giay, Hanoi, 10072, Vietnam


Aluminum hydroxide (ATH) is the most extensively used eco-friendly inorganic filler, offering both flame retardant and smoke inhibitory effects for a variety of polymers, including polyethylene, ethylene-propylene-diene monomer rubber (EPDM), ethylene vinyl acetate, epoxy, and polyvinyl chloride, *etc.*^{21–25} Research on the use of nanoparticles as flame retardant additives has made significant progress in addressing the challenges of high inorganic additive loading and poor dispersion. Notably, studies on using ATH nanoparticles as flame retardants have yielded promising results. In comparison to commercial ATH, ATH nanoparticles exhibit better dispersion and interaction with polymers, which improves the mechanical properties and fire resistance of nanocomposites.^{26–30} However, even in nanoparticle form, high loading of ATH is still necessary to achieve the desired flame retardant efficiency. Therefore, a combination of ATH with other flame retardants is crucial to create synergistic effects, reducing the overall amount of additives required.

Recently, some studies on the synergistic flame-retardant effect between PEI modified APP and other fillers have been reported. For instance, Liao *et al.*³¹ grafted APP with tannic acid (TA) using PEI as a bridging agent (TPAPP). When 10% TPAPP was added to polylactic acid (PLA), the limiting oxygen index (LOI) value of the composite increased from 20% (pure PLA) to 27.8%. APP@PEI was also combined with novel DOPO derivatives (DOPO – 9,10-dihydro-9-oxa-10-phosphaphenanthrene-10-oxide) in an EP matrix.³² The report indicated that some derivatives exhibited the good synergistic flame-retardant effect with APP@PEI. Wan *et al.*³³ prepared a new type of multi-layered nanomaterial coating APP, APP-PEI@MXene@ZIF-67. Subsequently, this material was introduced into thermoplastic polyurethane as a flame retardant filler. Compared with the pure polyurethane, the heat and smoke of the composite containing 20 wt% of this core-shell flame retardant released during combustion significantly reduced. Kang *et al.*³⁴ deposited APP and PEI into sisal fiber lumens by combining the water/nutrient transport mechanism of plant fiber with layer-by-layer self-assembly technology. When blending this modified fiber (30 wt%) with polypropylene, LOI value of the composite increased from 19.4% (unmodified) to 23.2%.

In this paper, aluminum hydroxide hexagonal nanoplates were synthesized using the hydrothermal method. Additionally, the surface of these nanoplates was treated with organic compounds, including oleic acid, Tween 80, and polyethyleneimine to improve their dispersion in an epoxy matrix. Next, EP nanocomposites were prepared by the thermal curing process, using ATH nanoplates and APP@PEI as flame retardant fillers. The flame retardancy, thermo-oxidative stability, and mechanical properties of these nanocomposites were investigated by the UL-94 vertical burning, limiting oxygen index test, thermal gravimetric analysis, tensile, and unnotched Izod impact measurements.

2 Experimental

2.1 Materials

Epoxy resin (LR 385, density: 1.16–1.20 g cm^{−3}, viscosity: 700–1050 mPa s, epoxy equivalent: 160–170 g per equivalent, epoxy

value: 0.58–0.64 equivalent/100 g) and hardener LH-386 (density: 0.93–0.97 g cm^{−3}, viscosity: 40–90 mPa s, amine value: 480–550 mg KOH per g) were bought from Hexion Specialty Chemicals, Germany. Commercial APP (form II) was supplied by China. Aluminum nitrate nonahydrate (Al(NO₃)₃·9H₂O, ≥98%), branched polyethyleneimine (PEI, 99%, MW 300), polysorbate 80 (Tween 80, micellar avg. mol. wt 79 000, average mol. wt 1310), and oleic acid (90%) were provided by Sigma-Aldrich. High-purity NaOH and absolute ethanol were used directly without additional purification.

2.2 Synthesis of aluminum hydroxide nanoplates

Aluminum hydroxide nanoplates (nATH) were synthesized using a hydrothermal method. The procedure was as follows: 60 g Al(NO₃)₃·9H₂O was dissolved in 640 mL distilled water to obtain a homogeneous solution. Next, 500 mL of 1 M NaOH was slowly dropped to this aluminum salt solution, and pH of the reaction mixture was maintained at 5. After stirring continuously for 1 h, the gel-like precipitates were collected by centrifugation and washed many times with water to remove the excess precursors. The resulting gel was then dispersed in 320 mL of 1 M NaOH solution to adjust the pH to 9. The mixture was transferred to a 500 mL Teflon vessel, which was sealed in a steel bomb reactor. This reactor was placed in a UM 400 Memmert electric oven (Germany) and heated to 80, 90, and 100 °C with a heating rate of 2 °C min^{−1}. The reaction systems were then maintained at the temperatures for 24–72 h. Finally, the white solid was obtained by centrifuging, washing several times with distilled water, and drying at 80 °C for 12 h.

2.3 Surface modification of aluminum hydroxide nanoplates

The surface of nATH was modified using oleic acid (OA), Tween 80 (Tw80), and PEI. The modifying agents (3% of the nATH mass) were dissolved in a certain amount of ethanol. Next, nATH powder was added to the solution and the mixture was continuously stirred at 60 °C for 2 h. The ethanol was then removed by rotary evaporation and the final products was labeled nATH_{OA}, nATH_{Tw80}, and nATH_{PEI}.

2.4 Preparation of APP@PEI

Ammonium polyphosphate was modified with polyethyleneimine (APP@PEI) based on previous literature.¹⁷ The preparation process of APP@PEI was carried out as follows: first, a solvent mixture was prepared by combining 210 mL ethanol and 10 mL distilled water. Then, 3.5 g PEI was completely dissolved in 20 mL of this solvent mixture under N₂ atmosphere. Meanwhile, 10 g APP and 200 mL the solvent mixture were added to a three-neck flask, stirred, and heated to 90 °C under N₂ atmosphere. Afterwards, the PEI solution was introduced into the flask, and the reaction system was continuously stirred at 90 °C for 2 h under N₂ atmosphere. The resulting white solid was then filtered and washed several times with ethanol to eliminate excess PEI. Finally, the sample was dried overnight in a vacuum oven at 80 °C to obtain APP@PEI powder.



2.5 Preparation of flame retardant epoxy nanocomposites

The EP composites were prepared through a traditional curing process, with a hardener to epoxy resin mass ratio of 34 : 100. The preparation involved the following steps: a certain amount of the flame retardant additives was dispersed in the hardener through stirring and ultrasonication. Afterwards, EP resin was added to the mixture with gentle stirring. When the mixture became homogeneous, it was poured into a silicone mold prepared according to standard dimensions of measurements. After curing at room temperature for 24 h and at 60 °C for 12 h, the EP composites were evaluated properties. The composite formulations are provided in Table 1.

2.6 Characterizations

UL-94 vertical combustion test (UL94-V) was carried on a GT-MC35F-2 horizontal and vertical flame chamber (Gester, China) based on ASTM D3801. Limiting oxygen index values were determined by using a Yasuda 214 oxygen index flammability tester (Japan) following ASTM D2863-13. The sizes of samples for both measurements were 125 mm × 13 mm × 3.2 mm.

The dispersion of nATH before and after the surface organization were observed using an Eclipse Ts2 Inverted Routine Microscope (Nikon, Japan). 3 wt% of nATH, nATH_{OA}, nATH_{Tw80}, or nATH_{PEI} were dispersed in the hardener by stirring and ultrasonication. Next, epoxy resin was added to the mixture and stirred until homogeneous. The mixture was then spread into a very thin layer on glass slides. They were cured at room temperature for 24 h and at 60 °C for 12 h before observation.

Fourier transform infrared (FT-IR) spectra were obtained on a L1600400 Spectrum two DTGS spectrometer (PerkinElmer, USA) by the KBr pellet method. The measurements were performed in a wavenumber range of 450–4000 cm^{−1} with a resolution of 1 cm^{−1}. X-ray diffraction (XRD) data were collected on a D8 Advance diffractometer (Bruker, Germany) using Cu K α radiation ($\lambda = 1.5406 \text{ \AA}$) source in a 2θ range from 10° to 70° with a step size of 0.02°.

Scanning electron microscopy (FE-SEM) and energy dispersive X-ray spectroscopy (EDX) measurements were conducted on an S-4800 instrument (Hitachi, Japan) at acceleration voltages of

5 kV and 20 kV, respectively. Before conducting SEM measurements, the nATH samples and the fracture surface of the nanocomposites were sputter coated with a platinum layer in an enclosed chamber for 40 s and 60 s, respectively, to enhance conductivity and image quality. The distribution of C, O, N, Al, and P elements in the nanocomposites was analyzed using an energy dispersive X-ray spectrometer (Horiba 7593-H) coupled with the SEM (SEM-EDX).

Thermogravimetric analysis (TGA) were carried out with a LABSYS Evo STA analyzer (Setaram, France) at a heating rate of 10 °C min^{−1} under an air atmosphere from 50 °C to 900 °C.

Tensile properties of epoxy composites were determined according to ISO 527 using a AI-7000M Testing Machine (Gotech, Taiwan) at a tensile rate of 20 mm min^{−1}. The tested specimens had dumbbell-shaped with a gauge length of 50 mm. Unnotched Izod impact strength of the materials were measured following ASTM D4812 using a mechanical test equipment (TestResources, USA). The samples had a dimension of 64 mm × 13 mm × 3 mm. The results for each formulation represented the average of five measurements, accompanied by error values.

3 Results and discussion

3.1 Morphology and structural characterization of nano aluminum hydroxide

Effect of hydrothermal temperature. The morphology and structure of aluminum hydroxide nanoplates synthesized at hydrothermal temperatures of 80, 90, and 100 °C for 72 h are presented. The resulting products were labeled nATH-1, nATH-2, and nATH-3. Fig. 1 depicts the XRD patterns of the nATH products obtained at these temperatures. The XRD pattern of nATH-1 reveals that the product is a mixture of two polymorphs including gibbsite (~77.7%) and bayerite (~22.3%), which are in good agreement with reference data (ICDD PDF #01-070-2038 and 01-077-0114, respectively). Meanwhile, XRD patterns of nATH-2 and nATH-3 illustrate the main diffraction peaks at $2\theta \sim 18.31^\circ$ (002) and 20.35° (200), suggesting that the products obtained at higher temperatures only consist of pure gibbsite with a high degree of crystallinity.

Table 1 Formulations of composites based on epoxy resin

| Samples | Compositions (wt%) | | | | | |
|--------------------------------|--------------------|---------|------|--------------------|----------------------|---------------------|
| | EP | APP@PEI | nATH | nATH _{OA} | nATH _{Tw80} | nATH _{PEI} |
| EP | 100 | — | — | — | — | — |
| 10APP@PEI/EP | 90 | 10 | — | — | — | — |
| 3nATH/7IFR ^a /EP | 90 | 7 | 3 | — | — | — |
| 3nATH _{OA} /7IFR/EP | 90 | 7 | — | 3 | — | — |
| 3nATH _{Tw80} /7IFR/EP | 90 | 7 | — | — | 3 | — |
| 3nATH _{PEI} /7IFR/EP | 90 | 7 | — | — | — | 3 |
| 1nATH _{PEI} /9IFR/EP | 90 | 9 | — | — | — | 1 |
| 5nATH _{PEI} /5IFR/EP | 90 | 5 | — | — | — | 5 |
| 10nATH _{PEI} /EP | 90 | — | — | — | — | 10 |

^a IFR: APP@PEI.



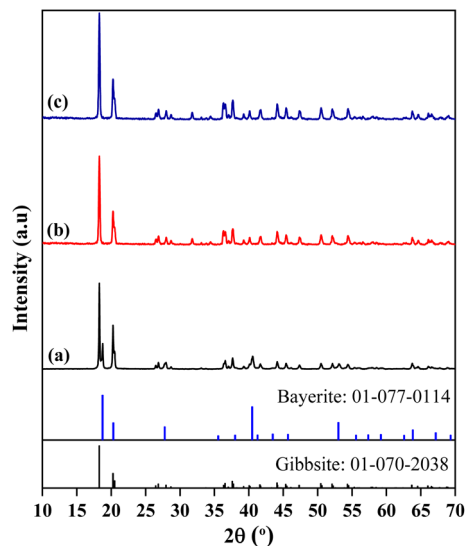


Fig. 1 XRD patterns of nano ATH synthesized at the different temperatures: (a) 80 °C, (b) 90 °C, and (c) 100 °C.

On the other hand, the hydrothermal temperature has also a strong impact on the morphology and particle size of nATH, as shown in Fig. 2. The product obtained at 80 °C is polygonal nanoplates with irregular sizes (Fig. 2a). At higher temperatures, the ATH crystals exist at the uniform hexagonal nanoplate structure. A statistical analysis of particle sizes from the SEM images indicates that the average particle diameter increases from 386 ± 21 nm at 90 °C (Fig. 2b and c) to 437 ± 26 nm at 100 °C (Fig. 2d). Nevertheless, the average thickness of the as-synthesized nATHs at 90 and 100 °C is the similar, approximately 30 nm. Additionally, as shown in Table 2, the reaction yield at 90 °C is the highest, approximately 82.5%. Based on

these results, the hydrothermal temperature of 90 °C was suitable for synthesizing ATH nanoplates with a high yield, uniform morphology, and consistent particle size.

Effect of crystallization time. The influence of various hydrothermal times (24 h, 48 h, and 72 h) at the reaction temperature of 90 °C is discussed. The corresponding products were labeled nATH-2, nATH-4, and nATH-5. As exhibited in Table 2, only a small amount of product is created after the reaction time of 24 h, which has a yield of 8.2%. The yield increases substantially, from 32.3% to 82.5%, when the synthesis time was extended from 48 h to 72 h. Fig. 3 shows XRD patterns of nano ATH obtained after different hydrothermal times. The XRD pattern of nATH obtained after a hydrothermal time of 24 h (nATH-4) reveals the initial formation of crystals, as indicated by the appearance of a broad diffraction peak at $2\theta \sim 18.31^\circ$ (Fig. 3a), which can be related to the (002) crystal face of gibbsite.³⁵ Meanwhile, the sharp diffraction peaks at $2\theta \sim 18.31^\circ$ and 20.35° observed in the XRD patterns of nATH-5 and nATH-2 confirm that the samples obtained after 48 h and 72 h are pure gibbsite (ICDD PDF #01-070-2038). SEM image of nATH obtained after 24 h shows that the sample still exists predominantly at the amorphous phase, and only a small portion transforming into the crystalline phase with an imperfect hexagonal nanoplate structure (Fig. 2e). This observation is consistent with the result of XRD analysis. In contrast, the morphologies of nATH obtained after 48 h and 72 h are entirely hexagonal nanoplates, with diameters from 345 to 386 nm (Fig. 2b, c and f). It can be seen that the particle size of the samples is insignificantly different, while the product yield obtained at 72 h is the highest. Hence, the hydrothermal temperature of 90 °C and the time of 72 h were selected to synthesize ATH nanoplates for the preparation of nano-composites based on epoxy resin.

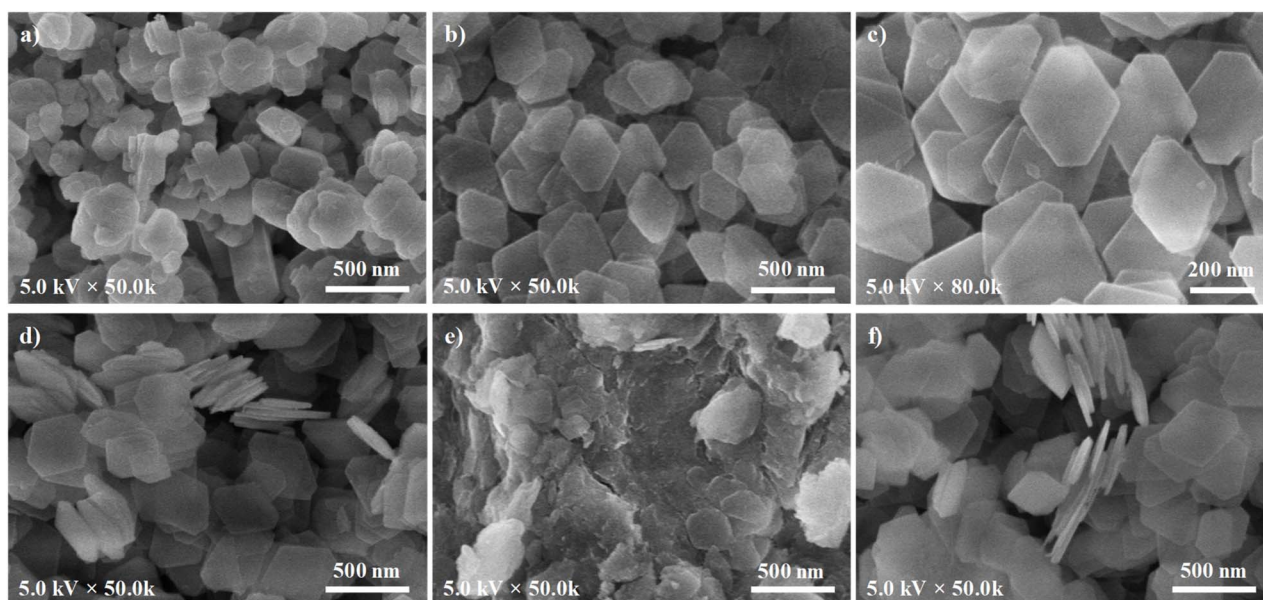


Fig. 2 SEM images of as-synthesized nano ATHs: nATH-1 (a), nATH-2 (b and c), nATH-3 (d), nATH-4 (e), and nATH-5 (f).



Table 2 Overview of nano ATH synthesis conditions and product characteristics

| Samples | Temp. (°C) | Time (h) | Product | Morphology | Yield (%) |
|---------|------------|----------|-----------------------------------|---|-----------|
| nATH-1 | 80 | 72 | 77.7% gibbsite, 22.3% bayerite | Polygonal nanoplates | 75.6 |
| nATH-2 | 90 | 72 | Gibbsite | Hexagonal nanoplates | 82.5 |
| nATH-3 | 100 | 72 | Gibbsite | Hexagonal nanoplates | 80.8 |
| nATH-4 | 90 | 24 | Amorphous gel with minor gibbsite | Amorphous with minor hexagonal nanoplates | 8.2 |
| nATH-5 | 90 | 48 | Gibbsite | Hexagonal nanoplates | 32.3 |

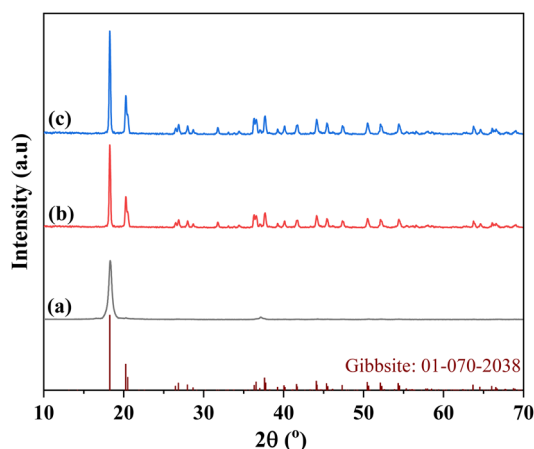


Fig. 3 XRD patterns of nano ATH synthesized at different hydro-thermal times: 24 h (a), 48 h (b), and 72 h (c).

3.2 Results of ATH nanoparticle surface modification

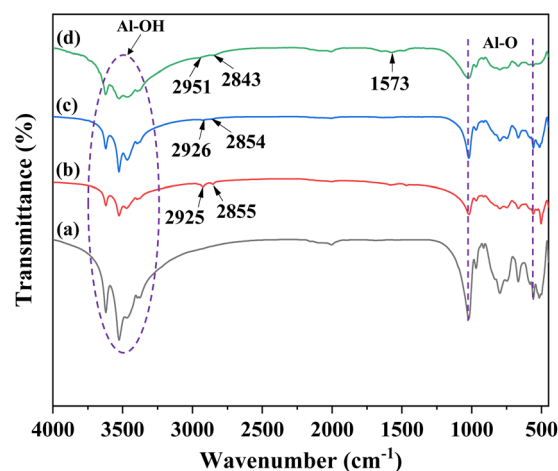
In order to improve the compatibility of the as-synthesized ATH nanoplates with polymer matrix, the surface of this material was treated by organic compounds. The FT-IR spectra of untreated nano $\text{Al}(\text{OH})_3$ (nATH), oleic acid-treated nATH (nATH_{OA}), Tween 80-treated nATH ($\text{nATH}_{\text{Tw80}}$), and PEI-treated nATH (nATH_{PEI}) are shown in Fig. 4. In all spectra, the characteristic absorption peaks of $\text{Al}(\text{OH})_3$ are observed at $3397\text{--}3623\text{ cm}^{-1}$ (O–H stretching vibrations), 1023 , and 559 cm^{-1} (Al–O stretching vibrations).³⁶ Furthermore, the FT-IR spectra of nATH_{OA} and $\text{nATH}_{\text{Tw80}}$ exhibit new peaks at about 2925 and 2855 cm^{-1} , attributed to the $-\text{CH}_2$ symmetric and asymmetric stretching vibrations,³⁷ respectively, in the structure of oleic acid and Tween 80. Meanwhile, peaks at 2951 and 2843 cm^{-1} in the FT-IR spectrum of nATH_{PEI} also correspond to the $-\text{CH}_2$ stretching vibrations in PEI. Additionally, a peak at 1573 cm^{-1} is assigned to the N–H bending vibrations of PEI.³⁸ These results indicate that the surface of ATH nanoplates is successfully coated with the modifying agents.

The dispersibility of nATH in the epoxy matrix before and after surface modification is illustrated in Fig. 5. It is evident that untreated ATH nanoplates tend to agglomerate into large clusters (Fig. 5a) due to their poor compatibility with the organic polymer matrix. However, the agglomerate of the nanoparticles is remarkably reduced after the surface modification. Among the tested samples, nATH_{PEI} demonstrates the

best dispersion within the polymer matrix, with distinct separation of nanoplates, as shown in Fig. 5d. This improvement is attributed to the surface modification of nATH with PEI which contains numerous amine groups ($-\text{NH}_2$, $-\text{NH}$) capable of reacting with the oxirane rings of the epoxy resin, thereby significantly enhancing the compatibility of nATH_{PEI} with the polymer. In addition, the dispersion of nATH_{PEI} in nanocomposites was observed by SEM-EDX mapping measurements. It can be seen that the Al elements in the $3\text{nATH}_{\text{PEI}}/7\text{IFR}/\text{EP}$ nanocomposite are concentrated in certain areas (Fig. 5e), suggesting the agglomerate of untreated nATH in the epoxy resin. In contrast, Fig. 5f manifests a uniform distribution of Al elements in $3\text{nATH}_{\text{PEI}}/7\text{IFR}/\text{EP}$, implying that nATH_{PEI} is well-dispersed in the intumescent flame retardant epoxy composite.

3.3 Flame retardancy

The flame retardancy of EP and its composites was evaluated using UL94-V and LOI tests, and the results are summarized in Table 3. EP is a combustible material, which burns out after the first ignition. The introduction of APP@PEI to epoxy resin significantly improved the fire resistance of the polymer. Specifically, the $10\text{APP@PEI}/\text{EP}$ composite passes a UL-94 V-0 rating, and its LOI value (28.9%) increases notably compared to the EP sample (21.1%). The flame retardant property of nanocomposites loading APP@PEI and nATH was

Fig. 4 FT-IR spectra of nATH before and after modification with organic compounds: (a) nATH, (b) nATH_{OA} , (c) $\text{nATH}_{\text{Tw80}}$, and (d) nATH_{PEI} .

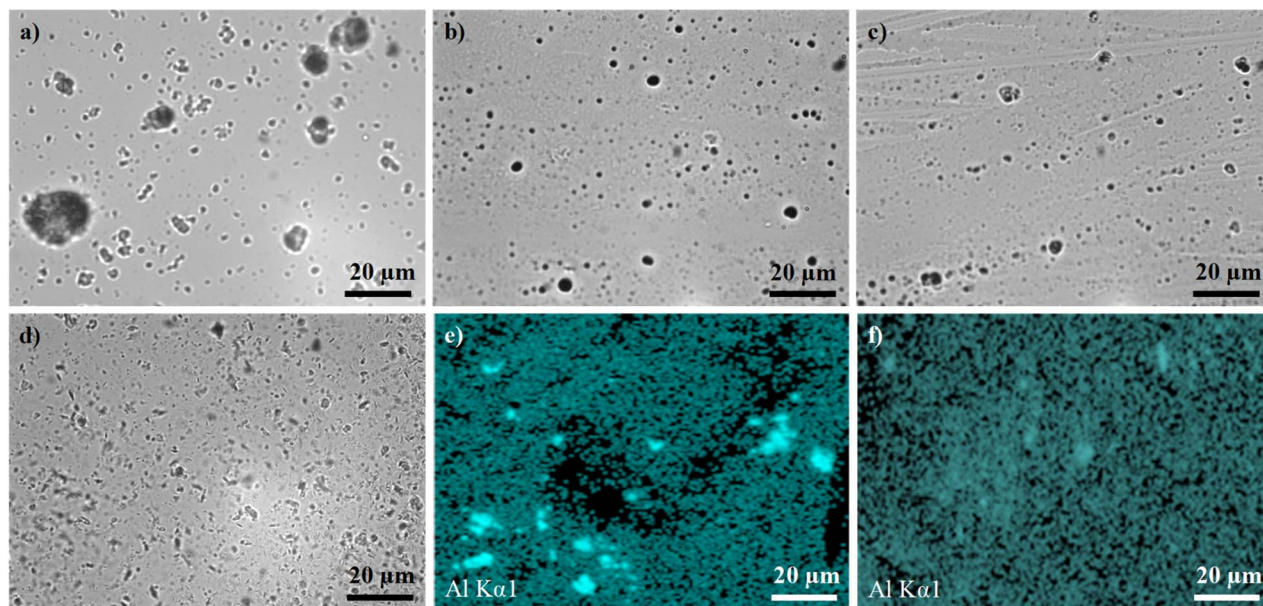


Fig. 5 Microscope images exhibit the dispersion of nATH before and after the surface modification in epoxy: nATH (a), nATH_{OA} (b), nATH_{Tw80} (c), and nATH_{PEI} (d); and aluminum distribution mapping in nanocomposites 3nATH/7IFR/EP (e) and 3nATH_{PEI}/7IFR/EP (f).

also investigated, with a sample total content of fillers (10 wt%). In comparison to the untreated nATH, the combination of APP@PEI and nATH surface-treated with the organic compounds enhances the flame retardancy of the composite. The flame resistance of 3nATH/7IFR/EP slightly diminishes compared to 10APP@PEI/EP, with a UL-94 V-1 rating and an LOI value of 28.5%. This result can be explained by the agglomeration of the untreated ATH nanoplates, which have high surface energy and poor compatibility with the organic polymer matrix. In contrast, the LOI values of 3nATH_{OA}/7IFR/EP, 3nATH_{Tw80}/7IFR/EP, and 3nATH_{PEI}/7IFR/EP increased to 30.7, 29.4 and 31.1%, respectively. It can be seen that PEI-treated nano ATH provides the highest fire retardant performance. This can be attributed to the good dispersion of nATH_{PEI} in epoxy resin, which is proved by the SEM-EDX mapping and microscope images (Fig. 5).

Additionally, the effect of nATH_{PEI} content on the flame retardancy of the composite containing APP@PEI was investigated. As indicated in Table 3, substituting a small amount of APP@PEI (≤ 3 wt%) with nATH_{PEI} results in a significant enhancement in the fire resistance of the composite. The self-extinguishing times after the flame applications in the UL94-V test notably reduce ($t_1 = 0.6$ s and $t_2 = 0.8$ s), and the LOI value grows to 31.1% when 3 wt% of APP@PEI is replaced with nATH_{PEI}. However, with a higher nATH_{PEI} content, the flame retardancy of the nanocomposite tends to diminish. The 5nATH_{PEI}/5IFR/EP nanocomposite achieves only a V-1 UL-94 rating ($t_1 = 3.1$ s and $t_2 = 15.4$ s) with an LOI value of 28.1%. The enhancement in flame resistance of the composite containing APP@PEI when combined with an appropriate amount of nATH_{PEI} is attributed to the synergistic flame retardant effect between APP@PEI and nATH.

Table 3 Flame retardance and mechanical properties of epoxy resin and its composites

| Samples | UL94-V (3.2 mm) | | | LOI (%) | Tensile strength (MPa) | Impact strength (kJ m ⁻²) |
|--------------------------------|-----------------|-------------|-------------|---------|------------------------|---------------------------------------|
| | Rating | t_1^a (s) | t_2^b (s) | | | |
| EP | NR ^c | Burnt out | — | 21.1 | 83.69 ± 0.2 | 45.92 ± 0.1 |
| 10APP@PEI/EP | V-0 | 3.3 | 5.8 | 28.9 | 59.84 ± 0.6 | 12.57 ± 0.3 |
| 3nATH/7IFR/EP | V-1 | 0.9 | 13.6 | 28.5 | 58.82 ± 0.7 | 14.54 ± 0.6 |
| 3nATH _{OA} /7IFR/EP | V-0 | 1.0 | 2.5 | 30.7 | 66.15 ± 0.3 | 21.54 ± 0.2 |
| 3nATH _{Tw80} /7IFR/EP | V-0 | 0.8 | 3.2 | 29.4 | 64.22 ± 0.5 | 19.83 ± 0.5 |
| 3nATH _{PEI} /7IFR/EP | V-0 | 0.6 | 0.8 | 31.1 | 67.80 ± 0.2 | 22.68 ± 0.1 |
| 1nATH _{PEI} /9IFR/EP | V-0 | 3.4 | 2.6 | 29.8 | 62.89 ± 0.1 | 20.15 ± 0.2 |
| 5nATH _{PEI} /5IFR/EP | V-1 | 3.1 | 15.4 | 28.1 | 68.44 ± 0.5 | 23.46 ± 0.4 |
| 10nATH _{PEI} /EP | NR | Burnt out | — | 22.8 | 71.65 ± 0.4 | 29.70 ± 0.3 |

^a t_1 : self-extinguishing time after the first ignition. ^b t_2 : self-extinguishing time after the second ignition. ^c NR: no rating.



3.4 Thermal oxidative behavior

TGA and DTG curves of EP and composites 10APP@PEI/EP, 10nATH_{PEI}/EP and 3nATH_{PEI}/7IFR/EP under air atmosphere are illustrated in Fig. 6, and the detailed data are summarized in Table 4. The EP resin undergoes two degradation stages under air atmosphere, with only 0.12 wt% remaining at 900 °C. For 10APP@PEI/EP, $T_{\max 1}$ and $T_{\max 2}$ values of this composite decrease significantly compared to the reference sample. However, the residue of 10APP@PEI/EP at 900 °C is approximately 14.75 wt%, much higher than that of the EP resin. These results can be attributed to the formation of phosphoric and polyphosphoric acids from the decomposition of APP. These acids then accelerate the decomposition of EP (dehydration and carbonization) to produce an intumescent char layer, which effectively protects the internal polymer matrix from the flame.¹⁵ In comparison with the EP resin, T_{onset} and $T_{\max 1}$ values of the 10nATH_{PEI}/EP nanocomposite decline by 5.34 and 17.19 °C, respectively. This reduction can be attributed to the endothermic dehydration of Al(OH)₃ at around 220 °C.^{22,28} However, $T_{\max 2}$ of this nanocomposite rises sharply by 40.28 °C.

Moreover, the char yield of 10nATH_{PEI}/EP at 900 °C is 7.62 wt%, slightly higher than the calculated residue of 6.63 wt%. These data suggest that the thermal oxidative stability of EP is enhanced by the addition of nATH_{PEI}. Compared to 10APP@PEI/EP, the T_{onset} value of the 3nATH_{PEI}/7IFR/EP nanocomposite shows a slight decrease. This phenomenon can be explained by the early decomposition of nano Al(OH)₃. However, the T_{\max} values of this nanocomposite are higher than

those of the 10APP@PEI/EP composite. Notably, the $T_{\max 2}$ value increases by approximately 20.61 °C. 3nATH_{PEI}/7IFR/EP also exhibits a reduced thermal decomposition rate and achieves higher char yield beyond 500 °C compared to 10APP@PEI/EP. This improvement can be attributed to the synergistic interaction between nATH_{PEI} and APP@PEI, which generates highly thermally stable aluminum phosphate compounds. These compounds reinforce the char structural surface of the nanocomposite, thereby effectively slowing the degradation of the nanocomposite at high temperatures. The results explain to the enhancement in the fire resistance of the 3nATH_{PEI}/7IFR/EP nanocomposite compared to the 10APP@PEI/EP composite.

3.5 Flame-retardant mechanism

Neat EP, 10nATH_{PEI}/EP, 10APP@PEI/EP, and 3nATH_{PEI}/7IFR/EP were calcined to 900 °C at a rate of 10 °C min⁻¹, using samples of the same weight. The char residues of samples were then analyzed using FT-IR, XRD, and EDX to investigate the synergistic flame-retardant effect between APP@PEI and nATH_{PEI}. Fig. 7 depicts the char structure of the samples after calcination. It can be observed that the char yield of neat EP remains insignificant (Fig. 7a), which agrees with the TGA data. By contrast, the introduction of flame retardants remarkably promotes char formation. Among flame-retardant composites, 10nATH_{PEI}/EP leaves the smallest char volume, however, its char structure is remarkably robust (Fig. 7b). The 10APP@PEI/EP composite forms a significantly larger porous char structure compared to 10nATH_{PEI}/EP (Fig. 7c). However, this char

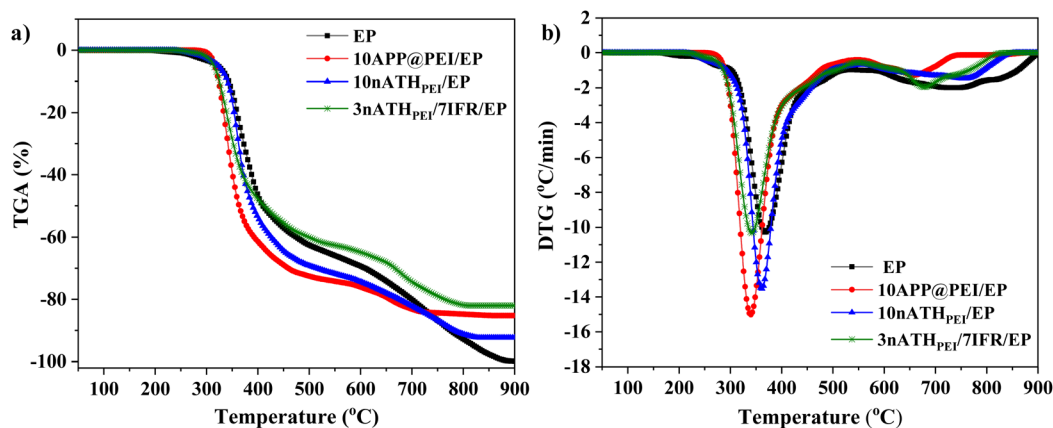


Fig. 6 TGA (a) and DTG (b) curves of EP and its composites under air atmosphere.

Table 4 TGA data of EP and its composites under air atmosphere

| Samples | T_{onset}^a (°C) | $T_{\max 1}^b$ (°C) | $T_{\max 2}^b$ (°C) | Residue at 900 °C (wt%) |
|-------------------------------|---------------------------|---------------------|---------------------|-------------------------|
| EP | 317.54 | 368.31 | 714.15 | 0.12 |
| 10APP@PEI/EP | 316.24 | 339.72 | 659.15 | 14.75 |
| 10nATH _{PEI} /EP | 312.2 | 351.12 | 754.43 | 7.62 |
| 3nATH _{PEI} /7IFR/EP | 314.21 | 341.65 | 679.76 | 17.98 |

^a T_{onset} : temperature at mass loss of 5 wt%. ^b T_{\max} : temperature at maximum degradation rate.

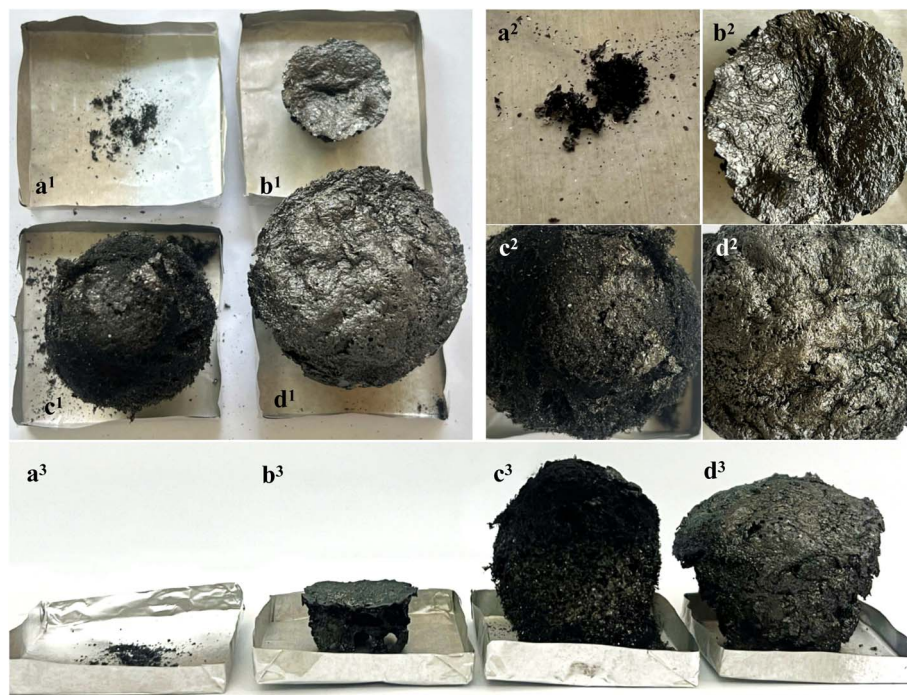


Fig. 7 Char structural images of EP and its composites after calcination at 900 °C: EP (a), 10nATH_{PEI}/EP (b), 10APP@PEI/EP (c), and 3nATH_{PEI}/7IFR/EP (d); superscript 1 and 2 illustrate the top view and 3 represents the side view of the residues.

layer is comparatively soft and prone to damage. The intumescence of the 3nATH_{PEI}/7IFR/EP nanocomposite after calcination is similar to that of the 10APP@PEI/EP composite; however, its char layer surface becomes noticeably more continuous and compact, as observed in Fig. 7d. The observation confirms that incorporating a small amount of nATH_{PEI} into the APP@PEI/EP composite helps to reinforce the char structure of the composite, effectively preventing the underlying materials from further combustion.

The chemical composition of char residues was analyzed by FT-IR, X-ray diffraction, and SEM-EDS. Fig. 8 illustrates FT-IR spectra and XRD patterns of the composites 10APP@PEI/EP, 10nATH_{PEI}/EP, and 3nATH_{PEI}/7IFR/EP after the calcination. As

displayed in Fig. 8A, all spectra appear peaks at 2926 and 2854 cm⁻¹ (–CH₂ stretching), 1744 cm⁻¹ (C=O stretching), and 1625 cm⁻¹ (C=C stretching),^{17,38–40} indicating that the aromatization and carbonization occur during the decomposition of the composites. In addition, the FT-IR spectrum of residues of 10APP@PEI/EP exhibits a peak at 1024 cm⁻¹ attributed to P–O stretching,^{8,41} suggesting the formation of the phosphorus-rich char structure upon the presence of APP@PEI. For 10nATH_{PEI}/EP, the FT-IR spectrum reveals the existence of alumina (Al₂O₃) at 1018–1163 cm⁻¹ (Al–O stretching) and 514 cm⁻¹ (O–Al–O bending),⁴² which is produced from the dehydration of nATH. However, the absorption peaks of Al₂O₃ disappear in the FT-IR spectrum of 3nATH_{PEI}/7IFR/EP. Instead, the intensity of the

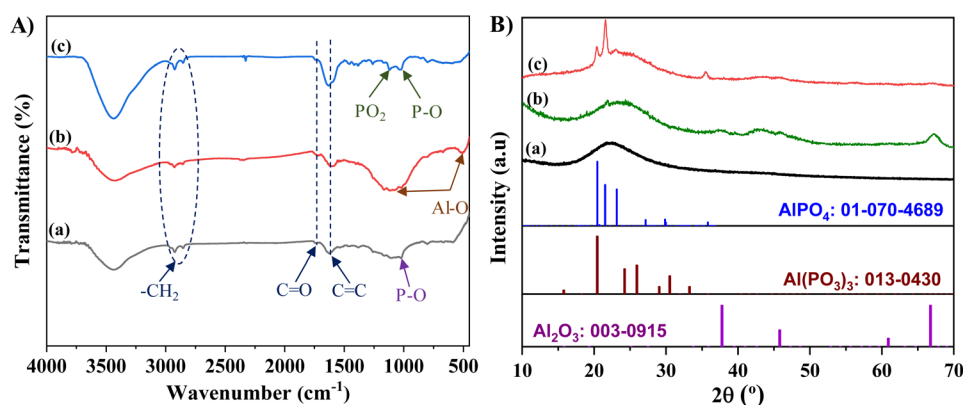


Fig. 8 FT-IR spectra (A) and XRD patterns (B) of char residues of 10APP@PEI/EP (a), 10nATH_{PEI}/EP (b), and 3nATH_{PEI}/7IFR/EP (c) after calcination at 900 °C.

absorption peak at 1030 cm^{-1} increases attributed to the overlap of P–O vibrations in char structure and a metal phosphate compound. Additionally, a new peak is observed at 1119 cm^{-1} , corresponding to PO_2 in a chain structure, where two oxygen atoms from the phosphorous bonded to aluminum atoms.⁴³ These findings demonstrate that, in addition to the phosphorus-rich char structure, metal phosphate compounds are formed during the combustion of the $3\text{nATH}_{\text{PEI}}/7\text{IFR}/\text{EP}$ nanocomposite through the interaction between the decomposition products of nATH and APP.

No discernible diffraction peaks are visible in the XRD pattern of residues of $10\text{APP}@/\text{PEI}/\text{EP}$, implying that the char structure of this material exists mainly in the amorphous phase. For $10\text{nATH}_{\text{PEI}}/\text{EP}$, the existence of Al_2O_3 in the residue is confirmed by peaks at $2\theta \sim 37.69^\circ$, 45.72° , and 67.24° (ICDD PDF #00-003-0915). However, the characteristic diffraction peaks of Al_2O_3 no longer exist in the char structure of $3\text{nATH}_{\text{PEI}}/7\text{IFR}/\text{EP}$. Instead, the XRD pattern of this char residue exhibits the appearance of aluminum orthophosphate (AlPO_4) at $2\theta \sim 20.32^\circ$, 21.60° , 22.91° , and 35.48° (ICDD PDF #01-070-4689). Additionally, a small amount of aluminum metaphosphate ($[\text{Al}(\text{PO}_3)_3]_n$) – a trivalent cation long chain polyphosphate could be formed in the char structure of this nanocomposite with the characteristic diffraction peak at $2\theta \sim 20.45^\circ$ (ICDD PDF #00-013-0430).^{44,45}

The result proves that the entire amount of Al_2O_3 produced by the dehydration of nATH reacts with decomposition products of APP to generate highly thermally stable aluminum phosphate compounds.

Fig. 9 depicts the results of SEM-EDX analyses of the char residues. To ensure uniform composition, the char residues of the composites were ground before conducting measurements. In addition to the similar char layer of the $10\text{APP}@/\text{PEI}/\text{EP}$

composite (Fig. 9a), new compounds are formed and primarily concentrated on the char structure of the $3\text{nATH}_{\text{PEI}}/7\text{IFR}/\text{EP}$ nanocomposite (Fig. 9c). This phenomenon aligns with the previously discussed XRD analysis, confirming the presence of aluminum phosphate crystals in the nanocomposite char structure. The EDX patterns identify elements such as C, O, P, and Al in the char. In contrast, the N element is absent from the char residues, suggesting that NH_3 and N-containing non-combustible gases are released during the material degradation process.^{46–48}

Based on the above discussions and previous studies, the flame retardant mechanism of the $3\text{nATH}_{\text{PEI}}/7\text{IFR}/\text{EP}$ can be described in Fig. 10. At low temperature, APP, PEI, and amine hardener of EP begin to decompose, releasing NH_3 and H_2O , which serves as a blowing gas for the intumescent flame-retardant system. Simultaneously, nano $\text{Al}(\text{OH})_3$ undergoes the endothermic decomposition, producing H_2O and Al_2O_3 . Subsequently, phosphoric acid and its poly-/ultra-/pyro-derivatives are generated through the chain scission of APP.^{49–51} These derivatives promote dehydration, esterification, and aromatization reactions between EP matrix and APP, resulting in a phosphorus – rich aromatic structure. Besides, part of phosphoric acid reacts with Al_2O_3 to create aluminum phosphates, such as AlPO_4 and $[\text{Al}(\text{PO}_3)_3]_n$, the highly thermally stable compounds. As the temperature increases, P–N–C groups are formed, but eventually decompose into N-containing non-combustible gases at higher temperatures.¹⁷ However, the P–O–P, C=C, C=O – containing aromatic ring structures remain in the char layer, and the presence of aluminum phosphates has the reinforcing effect this char structure. As a result, a better thermal stable char layer is formed, acting as a barrier that inhibits the heat transfer from the flame to the interior material and limits the diffusion of flammable decomposition products

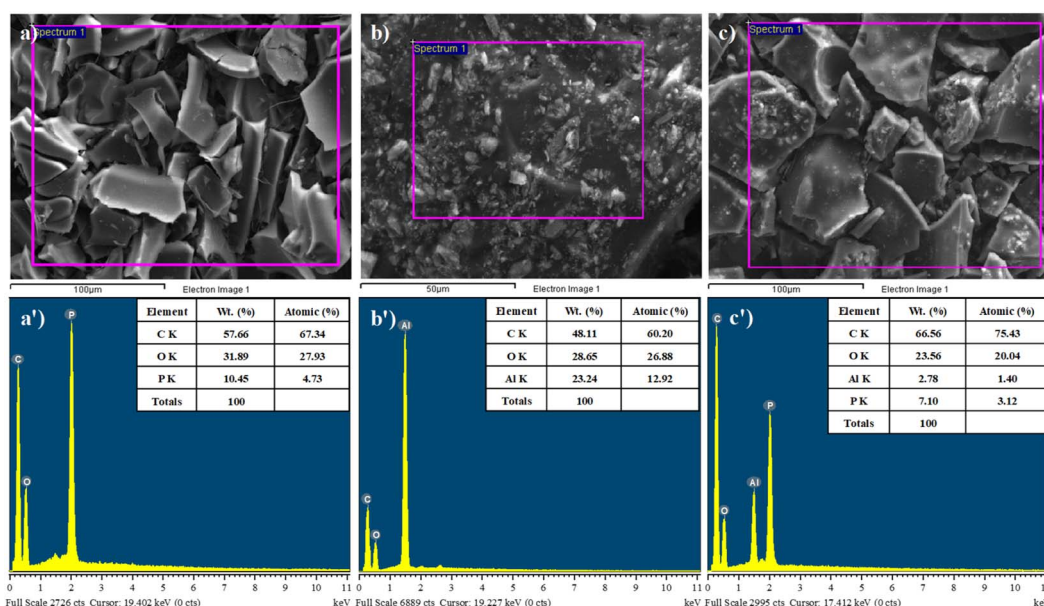


Fig. 9 SEM images and EDX spectra of the char residues of $10\text{APP}@/\text{PEI}/\text{EP}$ (a and a'), $10\text{nATH}_{\text{PEI}}/\text{EP}$ (b and b'), and $3\text{nATH}_{\text{PEI}}/7\text{IFR}/\text{EP}$ (c and c') after calcination at $900\text{ }^\circ\text{C}$.



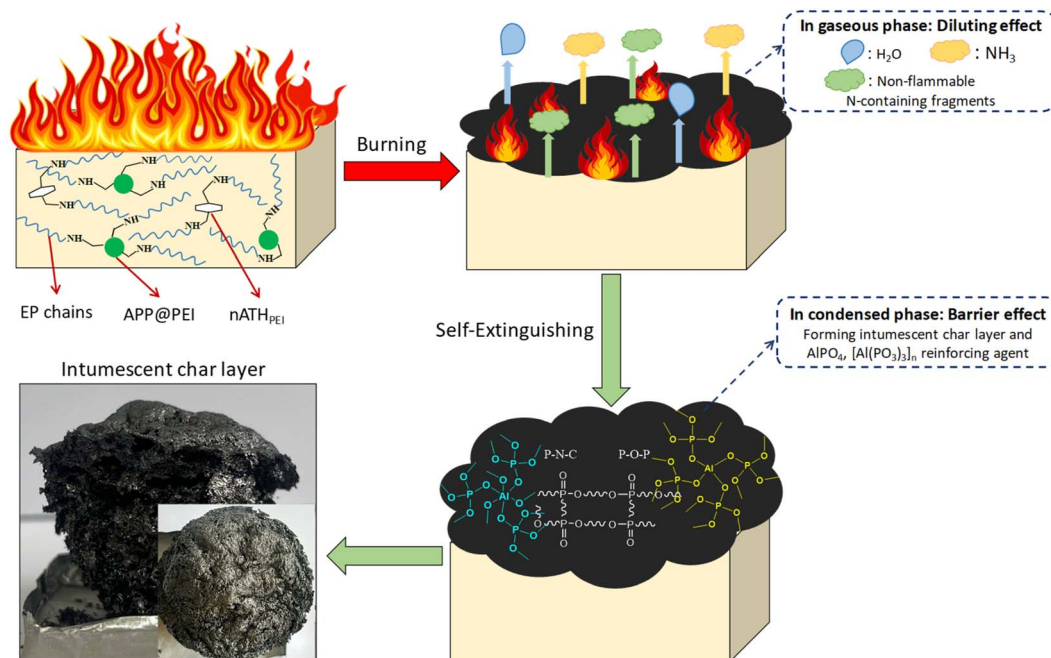


Fig. 10 Anticipated flame retardant mechanism of the nanocomposite 3nATH_{PEI}/7IFR/EP.

into the combustion zone. Therefore, the condensed-phase flame retardant mechanism of the nanocomposite demonstrates higher effectiveness.

3.6 Mechanical properties

Yield tensile and Izod impact strengths (unnotched) of EP resin and its composites are presented in Table 3. It is clear that incorporating APP@PEI negatively affects the mechanical properties of the EP resin. Specifically, the tensile and impact strengths of 10APP@PEI/EP are reduced by 28.50% and 72.63%, respectively, compared to the neat EP resin. Although the

compatibility of APP within the EP matrix improves after modification with PEI, clustering of the microparticles still occurs (Fig. 11a, b and d). Besides, the large particle size of this filler is another factor causing the deterioration in the mechanical properties of the composite. Replacing part of APP@PEI with untreated ATH nanoplates does not improve the mechanical performance of the composite. The agglomeration of the untreated ATH nanoplates is obviously observed in Fig. 5e and 11c. In addition, defects shown in Fig. 11c indicate the poor compatibility of this inorganic filler with the polymer matrix. As a consequence, the reinforcing property of the nanostructured

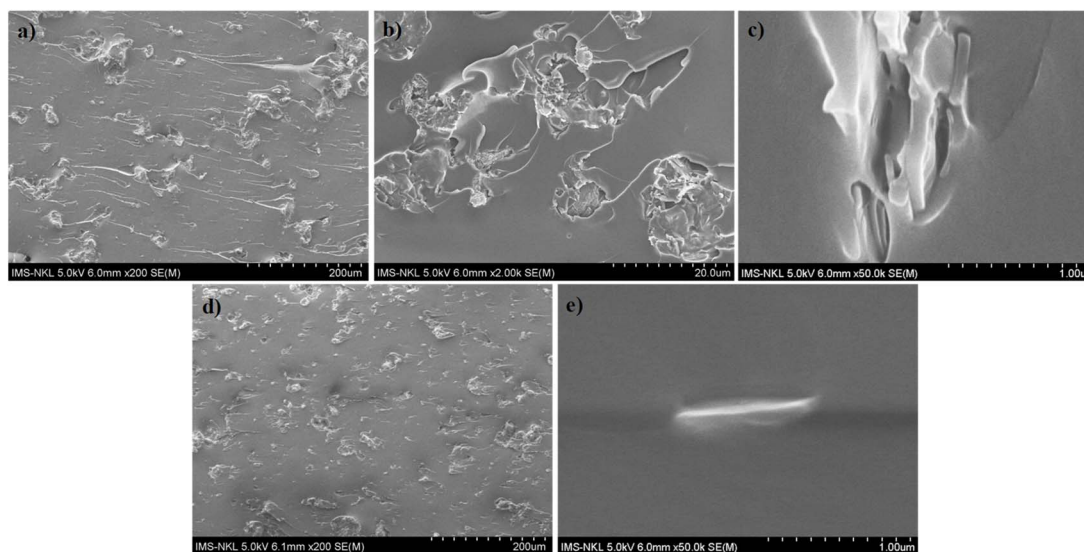


Fig. 11 The fracture surface images of 3nATH/7IFR/EP (a–c) and 3nATH_{PEI}/7IFR/EP (d and e) at different magnifications.



materials is not effectively harnessed. In contrast, the use of surface treated ATH nanoplates considerably enhances the mechanical properties of 10APP@PEI/EP. Among them, nATH_{PEI} provides the best reinforcement effect for the composite. The tensile and impact strengths of 3nATH_{PEI}/7IFR/EP heighten by roughly 13.30% and 80.43%, respectively, compared to 10APP@PEI/EP. Fig. 5f and 11e confirm the uniform dispersion of nATH_{PEI} within the nanocomposite. The good interfacial adhesion between the material with the EP matrix is also evident in Fig. 11e. These observations account for the improvement in mechanical properties of 3nATH_{PEI}/7IFR/EP. On the other hand, the influence of nATH_{PEI} content on the mechanical properties of nanocomposites was also evaluated. The results exhibit that both the tensile and impact strengths of the nanocomposites gradually grow as the proportion of APP@PEI replaced by nATH_{PEI} rises from 1 wt% to 10 wt%. Nevertheless, considering the discussions above, it can be concluded that the mixture of 3 wt% nATH_{PEI} and 7 wt% APP@PEI is the potential formulation for developing an epoxy nanocomposite system with high flame retardant efficiency and good mechanical property.

4 Conclusions

In summary, hexagonal gibbsite nanoplates were successfully prepared from an Al(OH)₃ gel precursor *via* a hydrothermal method. The average particle diameter and thickness of the as-synthesized nATH were approximately 350–450 nm and 30 nm, respectively. Additionally, these nanoplates were introduced into an intumescent flame-retardant epoxy system. It was found that PEI-treated nATH provided the best synergistic flame-retardant effect for the epoxy composite containing APP@PEI. Furthermore, the optimal content of nATH_{PEI} was also determined. As a result, the nanocomposite containing 3 wt% nATH_{PEI} and 7 wt% APP@PEI exhibited the highest fire resistance and thermal oxidative stability, achieving a UL-94 V-0 rating with a LOI value of 31.1% and a high char yield of 17.98% at 900 °C. The synergistic flame-retardant mechanism of the mixture of APP@PEI and nATH_{PEI} could be occurred in both the condensed and gaseous phases. In the condensed phase, APP@PEI promoted the formation of a phosphorus-rich char layer, which acted as a physical barrier to heat and mass transfer. Moreover, the interaction between nATH_{PEI} and APP@PEI produced aluminum phosphate compounds, which played a crucial role in reinforcing the char structure of the composite. In the gaseous phase, non-flammable gases could be released during decomposition, such as NH₃, H₂O, and other nitrogen-containing fragments, acted as blowing agents for the intumescent char layer and as inert diluents. Besides, the presence of nATH_{PEI} significantly improved the tensile and impact strengths of the composite loading APP@PEI.

Data availability

All data generated or analyzed during this study are included in the article. The datasets used and/or analyzed during the current study are available from the corresponding author upon

reasonable request. No restrictions apply to the data, and all data can be made available to the scientific community for future research upon request.

Author contributions

Conceptualization, Mai Ha Hoang; data analysis, Truong Cong Doanh, Nhung Hac Thi; methodology, Truong Cong Doanh, Nhung Hac Thi, Mai Ha Hoang; project administration, Mai Ha Hoang; validation, Hong Tham Nguyen, Ho Thi Oanh, Tien Dat Doan, Nguyen Duc Tuyen; writing – original draft, Truong Cong Doanh, Nhung Hac Thi; writing – review & editing, Mai Ha Hoang, Minh-Tan Vu, Truong Cong Doanh, and Nhung Hac Thi. All authors have read and agreed to the published version of the manuscript.

Conflicts of interest

There are no conflicts of interest to declare.

Acknowledgements

This research was supported by Vietnam Academy of Science and Technology under grant number KHCBBH.02/24-25.

References

- 1 Y. Yang, D.-Y. Wang, R.-K. Jian, Z. Liu and G. Huang, *Prog. Org. Coat.*, 2023, **175**, 107316.
- 2 B. Xu, Q. Zhang, H. Zhou, L. Qian and S. Zhao, *Composites, Part B*, 2023, **263**, 110832.
- 3 H. Niu, G. Wu, X. Wang, H. Ding and Y. Hu, *Polym. Degrad. Stab.*, 2023, **211**, 110333.
- 4 Y. Sui, X. Dai, P. Li and C. Zhang, *Macromol. Mater. Eng.*, 2021, **306**, 2100239.
- 5 Y. Sui, H. Sima, W. Shao and C. Zhang, *Composites, Part B*, 2022, **229**, 109463.
- 6 Y. Sui, X. Dai, P. Li and C. Zhang, *Eur. Polym. J.*, 2021, **156**, 110601.
- 7 Y. He, X. Cui, Z. Liu, F. Lan, J. Sun, H. Li, X. Gu and S. Zhang, *Polym. Degrad. Stab.*, 2023, **218**, 110579.
- 8 X. Chen, Y. Ma, S. Liu, A. Zhang, W. Liu and S. Huang, *Adv. Ind. Eng. Polym. Res.*, 2025, **8**, 48–62.
- 9 B. Xu, L. Shao, J. Wang, Y. Liu and L. Qian, *Polym. Degrad. Stab.*, 2020, **181**, 109281.
- 10 P. Wen, X. Feng, Y. Kan, Y. Hu and R. K. K. Yuen, *Polym. Degrad. Stab.*, 2016, **134**, 202–210.
- 11 S. Khanal, Y. Lu, S. Ahmed, M. Ali and S. Xu, *Polym. Test.*, 2020, **81**, 106177.
- 12 G. Turgut, M. Dogan, U. Tayfun and G. Ozkoc, *Polym. Degrad. Stab.*, 2018, **149**, 96–111.
- 13 B. Yuan, A. Fan, M. Yang, X. Chen, Y. Hu, C. Bao, S. Jiang, Y. Niu, Y. Zhang, S. He and H. Dai, *Polym. Degrad. Stab.*, 2017, **143**, 42–56.
- 14 Y. Zhan, X. Wu, S. Wang, B. Yuan, Q. Fang, S. Shang, C. Cao and G. Chen, *Polym. Degrad. Stab.*, 2021, **191**, 109684.



- 15 Y. Tan, Z. B. Shao, X. F. Chen, J. W. Long, L. Chen and Y. Z. Wang, *ACS Appl. Mater. Interfaces*, 2015, **7**, 17919–17928.
- 16 Y. Tan, Z.-B. Shao, L.-X. Yu, J.-W. Long, M. Qi, L. Chen and Y.-Z. Wang, *Polym. Chem.*, 2016, **7**, 3003–3012.
- 17 Y. Tan, Z.-B. Shao, L.-X. Yu, Y.-J. Xu, W.-H. Rao, L. Chen and Y.-Z. Wang, *Polym. Degrad. Stab.*, 2016, **131**, 62–70.
- 18 W.-J. Hu, Y.-M. Li, Y.-R. Li and D.-Y. Wang, *J. Therm. Anal. Calorim.*, 2022, **148**, 1841–1851.
- 19 F. N. Nguyen and J. C. Berg, *Composites, Part A*, 2008, **39**, 1007–1011.
- 20 A. M. Saks, J. C. Berg and F. N. Nguyen, *J. Adhes. Sci. Technol.*, 2007, **21**, 1375–1393.
- 21 Y. Pan, L. Han, Z. Guo and Z. Fang, *J. Appl. Polym. Sci.*, 2016, **134**, 44551.
- 22 N. H. Thi, T. N. Nguyen, H. T. Oanh, N. T. T. Trang, D. Q. Tham, H. T. Nguyen, T. Van Nguyen and M. H. Hoang, *J. Appl. Polym. Sci.*, 2020, **138**, e50317.
- 23 Y. Y. Yen, H. T. Wang and W. J. Guo, *J. Appl. Polym. Sci.*, 2013, **130**, 2042–2048.
- 24 M. Sabet, A. Hassan and C. T. Ratnam, *J. Reinf. Plast. Compos.*, 2013, **32**, 1122–1128.
- 25 J. F. Long, Z. L. Zhou, T. Wu, Y. Q. Li and S. Y. Fu, *Compos. Commun.*, 2023, **39**, 101562.
- 26 S. Elbasuney, *Powder Technol.*, 2017, **305**, 538–545.
- 27 V. K. Abitha, A. V. Rane, R. Uday, N. Samarth, A. V. Rane and V. Kamble, *Adv. Eng. Forum*, 2015, **14**, 3–18.
- 28 Z. Qin, D. Li, Q. Li and R. Yang, *Mater. Des.*, 2016, **89**, 988–995.
- 29 M. Ejaz, M. M. Azad, A. u. R. Shah, S. K. Afaq and J.-i. Song, *Cellulose*, 2022, **29**, 1775–1790.
- 30 R. Suchita, C. Mukesh, N. Manoj, B. Sneha, M. Smita and A. Anupam, *Int. J. Mater. Res.*, 2023, **114**, 678–688.
- 31 M. Liao, H. Chen, L. Deng, X. Wei, Z. Zou, H. Wang, S. Chen and Z. Zhu, *React. Funct. Polym.*, 2023, **192**, 105735.
- 32 C. T. Duc, L. C. Nguyen, P. B. Van, H. T. Nguyen, T. A. D. Thi, G. Le-Nhat-Thuy, Q. G. N. Thi, P. H. Thi, T. A. Nguyen, Q. V. Tran, H. T. Quang, M. H. Hoang and T. N. Van, *RSC Adv.*, 2024, **14**, 5264–5275.
- 33 M. Wan, C. Shi, L. Chen, L. Deng, Y. Qin, H. Che, J. Jing, J. Li and X. Qian, *Polym. Degrad. Stab.*, 2024, **226**, 110821.
- 34 F. Kang, H. Han, D. He, M. Yi, R. Wang and M. Zhou, *Ind. Crops Prod.*, 2025, **223**, 120176.
- 35 X. Zhang, X. Zhang, T. R. Graham, C. I. Pearce, B. L. Mehdi, A. T. N'Diaye, S. Kerisit, N. D. Browning, S. B. Clark and K. M. Rosso, *Cryst. Growth Des.*, 2017, **17**, 6801–6808.
- 36 X. Du, Y. Wang, X. Su and J. Li, *Powder Technol.*, 2009, **192**, 40–46.
- 37 S. Y. Qin, J. Feng, L. Rong, H. Z. Jia, S. Chen, X. J. Liu, G. F. Luo, R. X. Zhuo and X. Z. Zhang, *Small*, 2014, **10**, 599–608.
- 38 H. Liu, Y. Zhou, Y. Yang, K. Zou, R. Wu, K. Xia and S. Xie, *Appl. Surf. Sci.*, 2019, **471**, 88–95.
- 39 W. Song, X. Wang, Q. Wang, D. Shao and X. Wang, *Phys. Chem. Chem. Phys.*, 2015, **17**, 398–406.
- 40 J. Ding, S. Tang, X. Chen, M. Ding, J. Kang, R. Wu, Z. Fu, Y. Jin, L. Li, X. Feng, R. Wang and C. Xia, *Chem. Eng. J.*, 2018, **344**, 594–603.
- 41 S. Wang, Q. Fang, C. Liu, J. Zhang, Y. Jiang, Y. Huang, M. Yang, Z. Tan, Y. He, B. Ji, C. Qi and Y. Chen, *Eur. Polym. J.*, 2023, **187**, 111897.
- 42 A. Amirsalari and S. F. Shayesteh, *Superlattices Microstruct.*, 2015, **82**, 507–524.
- 43 K. Lertjiamratn, P. Praserttham, M. Arai and J. Panpranot, *Appl. Catal., A*, 2010, **378**, 119–123.
- 44 A. Castrovinci, G. Camino, C. Drevelle, S. Duquesne, C. Magniez and M. Vouters, *Eur. Polym. J.*, 2005, **41**, 2023–2033.
- 45 P. Khalili, K. Y. Tshai, D. Hui and I. Kong, *Composites, Part B*, 2017, **114**, 101–110.
- 46 Z.-B. Shao, C. Deng, Y. Tan, M.-J. Chen, L. Chen and Y.-Z. Wang, *Polym. Degrad. Stab.*, 2014, **106**, 88–96.
- 47 Z. B. Shao, C. Deng, Y. Tan, M. J. Chen, L. Chen and Y. Z. Wang, *ACS Appl. Mater. Interfaces*, 2014, **6**, 7363–7370.
- 48 Z.-B. Shao, C. Deng, Y. Tan, L. Yu, M.-J. Chen, L. Chen and Y.-Z. Wang, *J. Mater. Chem. A*, 2014, **2**, 13955–13965.
- 49 J. S. Wang, D. Y. Wang, Y. Liu, X. G. Ge and Y. Z. Wang, *J. Appl. Polym. Sci.*, 2008, **108**, 2644–2653.
- 50 J.-S. Wang, Y. Liu, H.-B. Zhao, J. Liu, D.-Y. Wang, Y.-P. Song and Y.-Z. Wang, *Polym. Degrad. Stab.*, 2009, **94**, 625–631.
- 51 L. Liu, Y. Zhang, L. Li and Z. Wang, *Polym. Adv. Technol.*, 2011, **22**, 2403–2408.

